Global fits of the cMSSM including the first LHC and XENON100 data

Gianfranco Bertone,[1, 2] David G. Cerdeño,[3] Mattia Fornasa *,[4]
Roberto Ruiz de Austri,[5] Charlotte Strege,[6] and Roberto Trotta[6, 7]

[1]*Institute for Theoretical Physics, Univ. of Zürich, Winterthurerst. 190, 8057 Zürich, CH*
[2]*Institut d'Astrophysique de Paris, UMR 7095-CNRS,*
Univ. Pierre & Marie Curie, 98bis Bd Arago 75014 Paris, France
[3]*Departamento de Física Teórica and Instituto de Física Teórica UAM-CSIC,*
Universidad Autónoma de Madrid, Cantoblanco, E-28049 Madrid, Spain
[4]*Instituto de Astrofísica de Andalucía (CSIC), E-18008, Granada, Spain*
[5]*Instituto de Física Corpuscular, IFIC-UV/CSIC, Valencia, Spain*
[6]*Astrophysics Group, Imperial College London, Blackett Laboratory, Prince Consort Road, London SW7 2AZ, UK*
[7]*African Institute for Mathematical Sciences, 6 Melrose Rd, Muizenberg, 7945, Cape Town, South Africa*
(Dated: July 12, 2011)

We present updated global fits of the constrained Minimal Supersymmetric Standard Model (cMSSM), including the most recent constraints from the ATLAS and CMS detectors at the LHC, as well as the most recent results of the XENON100 experiment. Our robust analysis takes into account both astrophysical and hadronic uncertainties that enter in the calculation of the rate of WIMP-induced recoils in direct detection experiment. We study the consequences for neutralino Dark Matter, and show that current direct detection data already allow to robustly rule out the so-called Focus Point region, therefore demonstrating the importance of particle astrophysics experiments in constraining extensions of the Standard Model of Particle Physics. We also observe an increased compatibility between results obtained from a Bayesian and a Frequentist statistical perspective. We find that upcoming ton-scale direct detection experiments will probe essentially the entire currently favoured region (at the 99% level), almost independently of the statistical approach used. Prospects for indirect detection of the cMSSM are further reduced.

I. INTRODUCTION

The constrained Minimal Supersymmetric Standard Model (cMSSM) [1, 2] is the most widely discussed extension of the Standard Model (SM) of particle physics. Despite its relative simplicity, this model has the advantage of capturing some key phenomenological feature of Supersymmetry (SUSY), while making definite predictions for the properties of the the lightest neutralino $\tilde{\chi}_1^0$ (which we denote χ here, for simplicity), a linear superposition of the superpartners of the neutral Gauge bosons and the neutral Higgses, which is by far the most popular Dark Matter (DM) candidate [3–6].

Recently, the ATLAS and CMS experimental collaborations have published the first search for supersymmetry (SUSY) [7–11], based on $\sqrt{s} = 7$ TeV proton-proton collisions at the LHC recorded during 2010 (see the experimental papers above for details on the event topologies, selection cuts, etc.). Since no excess above the SM predictions has been observed, these searches have set new interesting constraints on physics beyond the SM, and several groups of authors have already studied the impact of these results on the cMSSM and more in general on SUSY (see e.g. Refs. [12–15]).

Here, we perform new global fits of the cMSSM, following the methodology outlined in Refs. [16–18], where LEP constraints, precision tests of the SM and the most recent cosmological constraint on the relic abundance of the DM were implemented using nested sampling as a scanning algorithm, in order to derive both the most probable regions of the cMSSM (Bayesian) and the best fit regions (frequentist). We update the analysis to include new B-physics observables, as well as both the aforementioned LHC constraints and the upper limit on the WIMP-nucleon scattering cross-section arising from DM direct detection experiments (see e.g. Ref. [19] and references therein). We implement the findings of the XENON100 collaboration [20], which recently reported the results of a two-phase time projection chamber with 48 kg of liquid xenon as ultra-low background fiducial target. In 100.9 live days of data, acquired between January and June 2010, the collaboration recorded three candidate events, with an expected background of 1.8 ± 0.6 events. The rate of DM-induced recoil events in a direct detection experiment being directly proportional to the spin-independent scattering cross section of neutralinos off protons $\sigma_{\chi-p}^{\rm SI}$, the upper limit on the recoil rate translates into an upper limit on $\sigma_{\chi-p}^{\rm SI}$.

The predictions for $\sigma_{\chi-p}^{\rm SI}$ within the cMSSM (given constraints other than direct detection data) span approximately the range between 10^{-7} pb to 10^{-10} pb, and since XENON100 excludes $\sigma_{\chi-p}^{\rm SI}$ larger than 7.0×10^{-9} pb for a DM particle mass of 50 GeV at the 90% confidence level, one sees immediately that this has the potential to rule out significant portions of the cMSSM, under the hypothesis of a standard expansion rate of the Universe, and that the neutralinos make up most of the DM in the Universe.

Particular care must be paid, however, when translating the information provided by a direct detection experiment to constraints on the cMSSM parameter space, since this requires specific modeling of the velocity distribution of DM particles and of the DM density in the solar neighborhood. As a consequence, the upper limit from XENON100 can be considered robust only if the uncertainties on these quantities are taken into account. Moreover, the value of $\sigma^{\rm SI}_{\chi-p}$ depends on nuclear physics quantities, namely the hadronic matrix elements, which parametrize the quark composition of the proton, and this affects the way direct detection data are applied to constrain cMSSM parameters. Therefore in the present analysis we incorporate the local density, the quantities defining the DM velocity distribution and those modeling the proton composition as nuisance parameters, which are then either marginalized (i.e., integrated out) or maximised over to obtain inferences on the cMSSM parameters that fully account for those astrophysical and hadronic uncertainties.

The paper is organized as follows: in Section II we present our theoretical framework, in Section III we present the formalism for the computation of recoil events, our modelization of the DM velocity distribution and our implementation of the XENON100 data. Section IV is devoted to the presentation of the results, while prospects for the discovery of SUSY in the cMSSM are discussed in Section V. We conclude in Section VI.

II. THEORETICAL AND STATISTICAL FRAMEWORK

A. Model, priors and scanning algorithm

The five parameters defining a generic cMSSM are i) the coefficient of the universal mass term for scalars m_0 and ii) for gauginos $m_{1/2}$, iii) the coefficient of the trilinear interaction A_0, iv) the ratio between the vacuum expectation values of the Higgs bosons $\tan\beta$ and v) the sign of the mass term for Higges $\mathrm{sgn}(\mu)$. We consider only four of these in our scan, fixing the sign of the μ coefficient to be positive, a choice favoured by the results on the anomalous magnetic moment of the muon. The scanned range of the remaining four cMSSM parameters is summarized in Table I. Moreover, since residual experimental uncertainties on the value of some SM quantities can have strong effects on the values for the observables we are interested in [21], we also include in our scan the four SM parameters indicated in Table II, which are considered as nuisance parameters.

The cMSSM parameters together with the nuisance parameters in our scan are indicated by $\boldsymbol{\Theta}$. The core of Bayesian statistics is Bayes' theorem, which reads (see Ref. [27] for further details):

$$p(\boldsymbol{\Theta}|\mathbf{D}) = \frac{p(\mathbf{D}|\boldsymbol{\Theta})p(\boldsymbol{\Theta})}{p(\mathbf{D})}, \qquad (1)$$

cMSSM Parameters		
	Flat priors	Log priors
m_0 [GeV]	(50.0, 4000.0)	$(10^{1.7}, 10^{3.6})$
$m_{1/2}$ [GeV]	(50.0, 4000.0)	$(10^{1.7}, 10^{3.6})$
A_0 [GeV]	(-4000.0, 4000.0)	
$\tan\beta$	(2.0, 65.0)	

TABLE I: cMSSM parameters and the range covered on the scan. Flat priors are uniform in the masses, while log priors are uniform in the logarithm of the masses.

SM nuisance parameters			
	Gaussian prior	Range scanned	Ref.
M_t [GeV]	173.1 ± 1.3	(167.0, 178.2)	[22]
$m_b(m_b)^{\overline{MS}}$ [GeV]	4.20 ± 0.07	(3.92, 4.48)	[23]
$[\alpha_{em}(M_Z)^{\overline{MS}}]^{-1}$	127.955 ± 0.030	(127.835, 128.075)	[23]
$\alpha_s(M_Z)^{\overline{MS}}$	0.1176 ± 0.0020	(0.1096, 0.1256)	[24]
Astrophysical nuisance parameters			
$\rho_{\rm loc}$ [GeV/cm^3]	0.4 ± 0.1	(0.001, 0.900)	[25]
$v_{\rm lsr}$ [km/s]	230.0 ± 30.0	(80.0, 380.0)	[25]
$v_{\rm esc}$ [km/s]	544.0 ± 33.0	(379.0, 709.0)	[25]
v_d [km/s]	282.0 ± 37.0	(98.0, 465.0)	[25]
Hadronic nuisance parameters			
f_{Tu}	0.02698 ± 0.002	(0.010, 0.045)	[26]
f_{Td}	0.03906 ± 0.00395	(0.015, 0.060)	[26]
f_{Ts}	0.363 ± 0.119	(0.000, 0.085)	[26]

TABLE II: Nuisance parameters adopted in the scan of the cMSSM parameter space, indicating the mean and standard deviation adopted for the Gaussian prior on each of them, as well as the range covered in the scan. For scans in which the hadronic and/or astrophysical nuisance parameters have been held fixed, their value corresponds to the mean indicated here.

where $\mathbf{D}$ is the set of experimental data used to constraint the parameter space, while $p(\boldsymbol{\Theta}|\mathbf{D})$ on the l.h.s. of Eq. (1) is the posterior probability density function (pdf), $p(\mathbf{D}|\boldsymbol{\Theta})$ is the likelihood function (also indicated as $\mathcal{L}(\boldsymbol{\Theta})$) and $p(\boldsymbol{\Theta})$ is the prior pdf, representing our knowledge of the parameters before the data is taken into account. Bayes' theorem expresses how this prior information is updated by means of the experimental data through the likelihood function, so that the final pdf for $\boldsymbol{\Theta}$ depends both on the priors and on the likelihood. The evidence (or model likelihood) $p(\mathbf{D})$ only depends on the data so, for our purposes it represents a normalization factor and can thus be dropped. Different choices can be made for the prior probability in Eq. (1). However if the pdf at the end still exhibits a residual dependence on the priors, this represents a clear sign that the experimental data employed are not constraining enough to overcome the priors and, as a consequence, the resulting pdf should be considered with care [17, 28]. Following Refs. [17] and [18], in order to assess the robustness of our inference we consider two sets of priors: one that is uniform in the cMSSM masses ("flat" priors) and one that is uniform in their log ("log" priors). Both sets of priors are uniform

on A_0 and $\tan\beta$, and the ranges are indicated in Table I. For the SM, astrophysical and hadronic nuisance parameters our priors represents current available measurements of those quantities, and are indicated in Table II (further details are given in Section III B below). Furthermore, we also present results for the profile likelihood, which is in principle independent of the prior [18].

When presenting results for 1-dimensional or 2-dimensional subsets of the parameter space, the remaining parameters can be eliminated in two different ways:

- By marginalizing over them (i.e., integrating over – Bayesian), resulting in the 1-dimensional (or 2-dimensional) posterior pdf for the i-th parameter:

$$p(\Theta_i|\mathbf{D}) = \int p(\mathbf{\Theta}|\mathbf{D})d\Theta_1...d\Theta_{i-1}d\Theta_{i+1}d\Theta_n, \quad (2)$$

- By maximizing over them (i.e., profiling over the likelihood – Frequentist), resulting in the 1-dimensional (or 2-dimensional) profile likelihood function:

$$\mathcal{L}(\Theta_i) = \max_{\Theta_1,...,\Theta_{i-1},\Theta_{i+1},...,\Theta_n} \mathcal{L}(\mathbf{\Theta}). \quad (3)$$

Inferences resulting from those two approaches have, in general, a different meaning and may produce different results: the definition of the profile likelihood is more suited to determine possible small regions in the parameter space with large likelihood values, while, on the contrary, the pdf, integrating over hidden directions, correctly accounts for volume effects. Usually the largest amount of information on the structure of the scanned space derives from the comparison of the two [18, 28]. For both choices of priors, we use a modified version of the public SuperBayeS v1.5.1 package [29][1] to obtain posterior samples of Eq. (1), adopting MultiNest v2.8 [30, 31] as a scanning algorithm. We use running parameters as recommended in Ref. [18], namely a number of live points $n_{\text{live}} = 20,000$ and a tolerance parameter tol $= 10^{-4}$, which are tuned to obtain an accurate evaluation of the profile likelihood. Our final inferences for each of the log and flat priors are obtained from chains generated with approximately 13 (41) million likelihood evaluations for scans with fixed (varying) astrophysical and hadronic nuisance parameters, with an overall efficiency of about 5%. The profile likelihood plots are derived from merged chains from both of our log and flat priors scans, as advocated in Ref. [18], and are obtained from over 1 million samples.

B. The likelihood function

The experimental data $\mathbf{D}$ included in the likelihood are summarized in Table III. Observable quantities already included in Ref. [17] have been used here with the same likelihood function as in Ref. [17] (for the ALL setup), with updates to central values and standard deviations where applicable as indicated in Table III. In particular, we include LEP bounds on the Higgs mass, precision tests of the SM and an updated constraint on the DM relic density from WMAP 7-years data (assuming that neutralinos are the sole constituent of DM). We have also made the following modifications with respect to the treatment in Ref. [17]: the $BR(\bar{B} \to X_s\gamma)$ is now computed with the numerical code SusyBSG [40], which uses the full NLO QCD contributions, including the two-loop calculation of the gluino contributions presented in Ref. [42] and the results of Ref. [43] for the remaining non-QCD $\tan\beta$-enhanced contributions[2]. The other $B(D)$-physics observables summarized in Table III have been computed with the code SuperIso (for details on the computation of the observables see Ref. [39] and references therein). The anomalous magnetic moment of the muon, $\delta a_\mu^{\text{SUSY}}$, is also computed with SuperIso. Both SuperIso and SusyBSG have been integrated in a modified version of SuperBayeS v1.5.1.

In addition, we also include the recent constraints from SUSY searches at the LHC. We follow the analysis presented by the ATLAS collaboration in Ref. [44], since it is the one associated to the more stringent constraints: a data sample corresponding to a luminosity of 35 pb^{-1} for a center-of-mass energy of $\sqrt{s} = 7$ GeV is used to search for a SUSY signal in events with an isolated electron or muon with high transverse momentum, at least three hadronic jets and missing transverse momentum. No significant deviations are found with respect to SM predictions, and this is used to derive the constraints on the $(m_0, m_{1/2})$ plane indicated in Fig. 2 of Ref. [44] as a solid red line. We note that while this 95% exclusion line has been obtained assuming values of $\tan\beta = 3.0$ and $A_0 = 0$ GeV, the final result is not expected to change much for different values of these two parameters since it is obtained from decay channels that are fairly independent on the value of $\tan\beta$ and A. We include those exclusion limits by assigning a likelihood equal to zero to samples falling below the exclusion line.

The likelihood function for the direct detection constraints is a central ingredient of this work, and is presented in more detail in the next section.

---

[1] For this paper, the public SuperBayeS v1.5.1 code has been modified to interface with with DarkSUSY 5.0.5 [32, 33], SoftSUSY 2.0.18 [34, 35], MicrOMEGAs 2.0 [36, 37], SuperIso 2.4 [38, 39] and SusyBSG 1.4 [40, 41].

[2] For certain choices of the input parameters it may happen that the masses of two particles are accidentally close to each other. In some of these cases, this leads to numerical instabilities which usually are circumvented by compiling the program to quadruple precision. However, we have observed that in rare occasions numerical instabilities may persist.

Observable	Mean value	Uncertainties		Ref.
	μ	σ (exper.)	τ (theor.)	
M_W [GeV]	80.398	0.025	0.015	[45]
$\sin^2\theta_{eff}$	0.23153	0.00016	0.00015	[45]
$\delta a_\mu^{\rm SUSY} \times 10^{10}$	29.6	8.1	2.0	[46]
$BR(\bar{B} \to X_s\gamma) \times 10^4$	3.55	0.26	0.30	[47]
ΔM_{B_s} [ps^{-1}]	17.77	0.12	2.40	[48]
$\frac{BR(B_u\to\tau\nu)}{BR(B_u\to\tau\nu)_{SM}}$	1.28	0.38	-	[47]
$\Delta_{0-} \times 10^2$	3.6	2.65	-	[49]
$\frac{BR(B\to D\tau\nu)}{BR(B\to De\nu)} \times 10^2$	41.6	12.8	3.5	[50]
R_{l23}	1.004	0.007	-	[51]
$BR(D_s \to \tau\nu) \times 10^2$	5.38	0.32	0.2	[47]
$BR(D_s \to \mu\nu) \times 10^3$	5.81	0.43	0.2	[47]
$BR(D \to \mu\nu) \times 10^4$	3.82	0.33	0.2	[47]
$\Omega_\chi h^2$	0.1123	0.0035	10%	[52]

	Limit (95% CL)	τ (theor.)	Ref.
$BR(\bar{B}_s \to \mu^+\mu^-)$	$< 5.8 \times 10^{-8}$	14%	[53]
m_h	> 114.4 GeV (SM-like Higgs)	3 GeV	[54]
ζ_h^2	$f(m_h)$ (see Ref. [16])	negligible	[54]
$m_{\tilde{q}}$	> 375 GeV	5%	[23]
$m_{\tilde{g}}$	> 289 GeV	5%	[23]
other sparticle masses	As in table 4 of Ref. [16].		
$m_0, m_{1/2}$	LHC exclusion limits, see text		[44]
$m_\chi - \sigma_{\chi-p}^{\rm SI}$	XENON100 exclusion limits, see text		[20]

TABLE III: Summary of the observables used for the computation of the likelihood function Upper part: Observables for which a positive measurement has been made. $\delta a_\mu^{\rm SUSY} = a_\mu^{\rm exp} - a_\mu^{\rm SM}$ denotes the discrepancy between the experimental value and the SM prediction of the anomalous magnetic moment of the muon $(g-2)_\mu$. For each quantity we use a likelihood function with mean μ and standard deviation $s = \sqrt{\sigma^2 + \tau^2}$, where σ is the experimental uncertainty and τ represents our estimate of the theoretical uncertainty. Lower part: Observables for which only limits currently exist. The explicit form of the likelihood function is given in Ref. [16], including in particular a smearing out of experimental errors and limits to include an appropriate theoretical uncertainty in the observables. m_h stands for the light Higgs mass while $\zeta_h^2 \equiv g^2(hZZ)_{\rm MSSM}/g^2(hZZ)_{\rm SM}$, where g stands for the Higgs coupling to the Z and W gauge boson pairs.

III. CONSTRAINTS FROM DIRECT DETECTION DATA

A. Calculation of the recoil rate

Before discussing our implementation of direct detection results in the likelihood, we briefly review the calculation of the recoil rate, with particular emphasis on the astrophysical uncertainties (see also the discussion in Refs. [25, 55, 56]).

The rate of recoil events produced by DM interactions with a nucleus of mass m_N is given by

$$\frac{dR}{dE} = \frac{\rho_{\rm loc}}{m_\chi m_N}$$
$$\int_{\mathcal{V}} d\mathbf{v}\, v f(\mathbf{v} + \mathbf{v}_{\rm Earth}) \frac{d\sigma_{\chi-N}}{dE}(v, E). \quad (4)$$

Here, $\rho_{\rm loc}$ is the local DM density, $\mathbf{v}$ the DM velocity in the detector rest frame, $\mathbf{v}_{\rm Earth}$ the Earth velocity in the rest frame of the Galaxy, $f(\mathbf{w})$ the DM velocity distribution function and $d\sigma_{\chi-N}/dE$ is the differential cross section for the interaction between the neutralino and the nucleus. The integral is over the volume $\mathcal{V}$ of phase space

for which v is smaller than the escape velocity $v_{\rm esc}$ and larger than the minimal velocity $v_{\rm min}(E)$ able to produce a recoil with energy E: $v_{\rm min}(E) = \sqrt{m_N E/2\mu_N^2}$, where $\mu_N = m_\chi m_N(m_\chi + m_N)^{-1}$ is the neutralino-nucleus reduced mass.

We will focus here only on the case of spin independent (SI) interaction, assuming also that protons and neutrons are characterized by the same cross section. Therefore:

$$\frac{d\sigma_{\chi-N}}{dE}(v, E) = \frac{m_N}{2\mu_p^2 v^2}\sigma_{\chi-p}^{\rm SI}\sum_i \omega_i A_i^2 F_i^2(A_i, E), \quad (5)$$

where μ_p is the neutralino-proton reduced mass. The sum is over all the isotopes present in the detector, each one with its own abundance factor ω_i. A_i is the atomic mass number of the i-th nuclear species and $F(A_i, E)$ the nuclear form factor, which we have taken from Ref. [57].

B. Astrophysical and hadronic nuisance parameters

Regarding the velocity distribution function entering Eq. (4), we account for uncertainties in the halo model

by considering the following parametrization:

$$f(\mathbf{v}) = f_0 \left[\exp\left(\frac{3(v_{\text{esc}}^2 - v^2)}{2v_d^2} \right) - 1 \right]^k. \qquad (6)$$

The distribution function depends on three parameters, (k, v_{esc}, v_d), and f_0 is simply a normalization factor. Eq. (6) has been introduced in Ref. [58] as an *Ansatz* able to reproduce the phase space structure of N-body simulated DM halos and, compared to the standard Maxwellian distribution, it predicts a smaller number of DM particle in the high velocity tail, which entails less recoil events. For simplicity we reduce the number of parameters in the velocity distribution function to just two, fixing throughout $k = 1$.

From Eqs. (4) and (6), astrophysics affects the number of predicted recoil events through the dependence on the three velocities (v_{Earth}, v_{esc}, v_d) and the local density ρ_{loc}. As done in Ref. [25], we note that v_{Earth} can be reasonably approximated by the value of the local circular velocity, v_{lsr}, so we assume $v_{\text{Earth}} = v_{\text{lsr}}$. The value of these "astrophysical nuisance parameters" is constrained using a Gaussian prior with mean and standard deviation as motivated in Ref. [25], and given in the central part of Table II. In order to derive a prior for the velocity dispersion, v_d, we use the relationship $v_d = \sqrt{3/2}v_0$ and, as in Ref. [25], the mean velocity v_0 is assumed to be equal to v_{lsr}. However, in our scans we allow both v_d and v_{lsr} to vary as free, independent parameters (in order to be conservative), within the range given in Table II.

Finally, $\sigma_{\chi-p}^{\text{SI}}$ is proportional to the square of the effective coupling of the neutralino to the proton, f_p:

$$\frac{f_p}{m_p} = \sum_{q=u,d,s} f_{Tq} \frac{\alpha_q^s}{m_q} + \frac{2}{27} f_{TQ} \sum_{q=u,d,s} \frac{\alpha_q^s}{mq}, \qquad (7)$$

where the quantities f_{Tq} represent the contributions of the light quarks to the mass of the proton, and are defined as $f_{Tq} = m_p \langle p | m_q \bar{q}q | p \rangle$. The second term corresponds to the interaction of the neutralino with the gluon scalar density in the proton, with $f_{TQ} = 1 - \sum_{q=u,d,s} f_{Tq}$. The coefficients α_q^s correspond to the neutralino-quark scalar couplings in the low-energy effective Lagrangian and are calculated for each point in our scan. The hadronic matrix elements f_{Tq} are determined experimentally in nuclear measurements and the uncertainty in their value (especially that on f_{Ts}) has a direct impact on the computed cross section. We therefore consider them as nuisance parameters in the scan and we constrain them with an informative Gaussian prior, with mean and standard deviation as indicated in Table II, taken from [26].

C. Implementation of XENON100 data

We have now assembled all the necessary elements to implement the constraints from direct detection experiments to our likelihood. The most stringent results to date have been recently obtained by the XENON100 experiment, which is located at the Laboratori Nazionali del Gran Sasso in Italy. DM is searched for with a target of dual-phase (liquid/gas) xenon in an environment of extremely low background. A particle interacting with the detector produces a primary scintillation signal $S1$ in the liquid xenon. Subsequently, ionization electrons drift towards the region with gaseous xenon producing the secondary scintillation signal $S2$. The background is largely reduced by considering only single scattering events, while the $S2/S1$ ratio is employed to discriminate nuclear recoils (produced by backgrounds or candidate WIMPs event) from electronic recoils (from γ or β background).

The latest results [20] have been obtained with an effective volume of 48 kg and 100.9 days of exposure. The signal region is defined by a series of quality cuts determined blindly, in an energy window between 8.4 and 44.6 keV, from the requirement of having from 4 to 30 photoelectron events (PE). In this region, 3 events have been detected with energies of 12.1 keV, 30.2 keV and 34.6 keV. The expected number of events from the background is $b = 1.8 \pm 0.6$. In our analysis, we adopt a fixed central value for the background. We have checked that marginalizing over the background uncertainty has a negligible impact on our results.

In this work, we do not employ the energy distribution of the observed events, but only their total number. Having observed $\hat{N} = 3$ events and with an expected background of b events, the likelihood function for the parameters $\mathbf{\Theta}$ is a Poisson distribution (up to a normalization constant, L_0)

$$\mathcal{L}_{\text{Xe100}}(\mathbf{\Theta}) \propto p(\hat{N}|\lambda) = L_0 \frac{\lambda^{\hat{N}}}{\hat{N}!} e^{-\lambda}, \qquad (8)$$

where $\lambda = s(\mathbf{\Theta}) + b$ and the expected signal $s(\mathbf{\Theta})$ is obtained as described below. The normalization constant L_0 is chosen in such a way that $\ln \mathcal{L}_{\text{Xe100}} = 0$ when $\lambda = \hat{N}$, i.e., when the predicted signal plus the expected background match the observed number of counts. The probability distribution of the number of PE events, n, is obtained by convolving the differential recoil rate with a Poisson distribution with mean $S1(E)$, accounting for the acceptance cuts and other quality cuts of the data via a function $\zeta(E)$:

$$\frac{\mathrm{d}R}{\mathrm{d}n} = \int_0^\infty \frac{\mathrm{d}R}{\mathrm{d}E} \zeta(E) P(n|S1(E)) \mathrm{d}E, \qquad (9)$$

where $\zeta(E)$ is a function parameterizing the acceptance of all data quality cuts, $P(n|S1(E))$ is a Poisson distribution for n with mean $S1(E)$, and

$$S1(E) = L_y \frac{S_{\text{nr}}}{S_{\text{ee}}} E L_{\text{eff}}(E) \qquad (10)$$

gives the number of PE produced by an event with recoil energy E (we neglect the uncertainty due to the

finite single-electron resolution of the photomultipliers, which is small, $\sigma_{\mathrm{PMT}} = 0.5$ PE). In the above equation, $S_{\mathrm{nr}} = 0.95$ and $S_{\mathrm{ee}} = 0.58$ are the scintillation quenching factors for nuclear and electronic recoils, respectively; $L_y = 2.20 \pm 0.09$ PE/keV$_{\mathrm{ee}}$ is the light yield (whose uncertainty we neglect, as it is small) and $L_{\mathrm{eff}}(E)$ is the scintillation efficiency, which we take to be the best fit line in Fig. 1 of [20]. We neglect the uncertainty in $L_{\mathrm{eff}}(E)$, which however is only important for very light WIMP mass, $m_\chi < 10$ GeV, as argued recently in Ref. [59]. As such small values of the neutralino mass are not realized in the cMSSM, our assumption has a negligible impact on our results. The expected total number of events is obtained by summing over all possible number of PE reaching the photomultipliers, within the acceptance window $\mathrm{PE}_{\mathrm{min}} = 4$ and $\mathrm{PE}_{\mathrm{max}} = 30$:

$$s = \sum_{n=\mathrm{PE}_{\mathrm{min}}}^{\mathrm{PE}_{\mathrm{max}}} \epsilon \frac{\mathrm{d}R}{\mathrm{d}n}, \qquad (11)$$

where ϵ is the exposure. We make the further simplification of assuming an energy-independent ζ, and for the combined value of $\zeta\epsilon$ we take the effective (post-cuts) exposure of 1481 kg days [20].

We have checked that the above simplified treatment reproduces fairly accurately the exclusion limit obtained in Ref. [20] in the $m_\chi - \sigma_{\chi-p}^{\mathrm{SI}}$ plane. As we do not make use of spectral information, we expect our limit to be more conservative than the one derived using the more sophisticated likelihood in Ref. [20, 60]. Indeed, for the same choice of astrophysical nuisance parameters as in Ref. [20], we find a 90% limit $\sigma_{\chi-p}^{\mathrm{SI}} = 0.85 \times 10^{-8}$ pb for a WIMP mass $m_\chi = 50$ GeV, which is to be compared with the tighter limit found in Ref. [20], $\sigma_{\chi-p}^{\mathrm{SI}} = 0.70 \times 10^{-8}$ pb.

IV. RESULTS

A. Impact of LHC data

We start by showing in Fig. 1 the impact of the new LHC results on the posterior pdf (for both choices of priors) and the profile likelihood of the cMSSM. As one can see by comparing the empty grey contours (without LHC data) with the black contours (including LHC limits), the impact of current LHC limits is actually fairly modest, since the largest part of the favoured region under the remaining data is located at larger values of m_0 and $m_{1/2}$ (see also Refs. [61, 62] for a more detailed analysis).

The posterior pdf's in this figure exhibit the familiar features of the cMSSM (see e.g. the discussion in Ref. [17]). We observe in particular two distinct areas in the $m_0, m_{1/2}$ plane: the neutralino-stau coannihilation region, that appears as a narrow band for small scalar masses, and a wide area which extends to sizable scalar masses, corresponding to the so-called focus point (FP) region [63, 64] (also know as hyperbolic branch [65]). The

latter is particularly prominent in the case of flat priors (top panels), due to the "volume effects" associated with this prior discussed in Ref. [17]. Along the FP branch the absolute value of the μ parameter is of order of the electroweak scale despite scalar particles being very massive (generally several TeV), as long as gaugino masses are not too large. The smallness of μ has been interpreted as corresponding to low values of the fine-tuning of the model and is due to a "focused" behaviour of the Renormalization Group Equation for the Higgs mass parameters.

This FP region has interesting consequences for the nature of the dark matter. Since μ is of the same order as the gaugino mass parameters, the neutralino exhibits a significant Higgsino fraction (it is a mixed Higgsino-bino state). As a consequence its relic density decreases [66], making it possible to satisfy the experimental constraint on the abundance of dark matter. The increased Higgsino fraction also leads to a large spin-independent neutralino-nucleon cross section, since Higgs exchange along a t-channel becomes more effective (it is proportional to the product of Higgsino and gaugino components). The cross section can thus be as large as $\sigma_{\chi-p}^{\mathrm{SI}} \sim 10^{-8}$ pb for neutralino masses as large as 1 TeV, and in fact the focus point region is easily identified in the $m_\chi \sigma_{\chi-p}^{\mathrm{SI}}$ plane (see the top right panel of Fig. 1) as a plateau in the region $\sigma_{\chi-p}^{\mathrm{SI}} \sim 10^{-7} - 10^{-8}$ pb.

As we shall see, the latest XENON100 direct detection data set stringent constraints on this region. This can already be seen from the right most panels in Fig. 1, which display the constraints (without inclusion of direct detection data) in the plane spanned by m_χ and $\sigma_{\chi-p}^{\mathrm{SI}}$: especially for the flat prior case, the FP region appears as a sizable island of high probability above the dashed red line, which represents the 90% limit from the most recent XENON00 data (for standard astrophysical assumptions – we shall relax those in the next section). Therefore we expect that the inclusion of the direct detection constraints will further reduce the viability of the FP region, as we demonstrate below.

Turning now to the profile likelihood results (bottom panels in Fig. 1), we see that the FP region is excluded at the 95% level, but still viable at the 99% level (outer-most black contours), which we are able to map out thanks to our high-resolution scan. Most of the favoured region however lies below ~ 1 TeV for both the scalar and gaugino masses. As a consequence, we observe in the $m_\chi - \sigma_{\chi-p}^{\mathrm{SI}}$ (bottom right panel) that the cMSSM parameter above the current nominal XENON100 limit is for the most part disfavoured at the 99% level from a profile likelihood perspective. We also point out that the 99% region from the profile likelihood is much wider than could be assumed just by qualitatively extending either the 68% or the 95% range, and this owing to the highly non-Gaussian nature of the tails of the distribution. Our results therefore indicate that a high-resolution scan is necessary to map out the tails of the profile likelihood with sufficient accuracy in order to delimit the

	Fixed nuisance		Incl. nuisance	
	Flat priors	Log priors	Flat priors	Log priors
Input parameters				
m_0 [GeV]	108.52	88.68	220.51	98.26
$m_{1/2}$ [GeV]	390.96	370.54	582.41	363.28
A_0 [GeV]	-326.06	-286.55	990.39	-278.95
$\tan\beta$	13.94	11.10	24.29	13.48
M_t [GeV]	173.383	173.129	173.209	173.617
$m_b(m_b)^{\overline{MS}}$ [GeV]	4.210	4.236	4.212	4.271
$[\alpha_{em}(M_Z)^{\overline{MS}}]^{-1}$	127.956	127.968	127.959	127.961
$\alpha_s(M_Z)^{\overline{MS}}$	0.118	0.119	0.117	0.117
Observables				
m_h [GeV]	115.1	114.2	114.7	114.5
m_χ [GeV]	157.6	148.5	238.8	145.6
$\delta a_\mu^{SUSY} \times 10^{10}$	18.54	17.22	29.20	20.89
$BR(\bar{B} \to X_s\gamma) \times 10^4$	3.83	3.36	3.16	3.59
$\Delta_{0-} \times 10^2$	8.78	8.42	8.25	8.45
$BR(D_s \to \tau\nu) \times 10^2$	4.82	4.82	4.82	4.82
$BR(D \to \mu\nu) \times 10^4$	3.86	3.86	3.86	3.86
$\sigma_{\chi-p}^{\rm SI}$ [pb]	3.2×10^{-9}	3.5×10^{-9}	4.0×10^{-9}	3.5×10^{-9}
$\sigma_{\chi-p}^{\rm SD}$ [pb]	8.0×10^{-7}	1.1×10^{-6}	7.9×10^{-7}	1.1×10^{-6}
$\Omega_\chi h^2$	0.1142	0.1142	0.1096	0.1105

TABLE IV: Best fit points for the flat and log prior scans. The columns "Fixed nuisance" are for the case where astrophysical and hadronic parameters have been fixed to their fiducial values, while "Incl. nuisance" denotes the case where they have been included in the scan and profiled over.

	Fixed nuisance		Incl. nuisance	
Observable	Flat priors	Log priors	Flat priors	Log priors
SM nuisance	0.204	0.750	0.087	1.247
Astro nuisance	N/A	N/A	1.060	0.522
Hadronic nuisance	N/A	N/A	0.630	0.667
M_W	0.986	1.072	1.037	0.828
$\sin^2\theta_{eff}$	0.105	0.900	0.096	0.150
δa_μ^{SUSY}	1.755	2.202	0.002	1.089
$BR(\bar{B} \to X_s\gamma)$	0.527	0.228	0.964	0.008
ΔM_{B_s}	0.274	0.262	0.276	0.315
$\frac{BR(B_u \to \tau\nu)}{BR(B_u \to \tau\nu)_{SM}}$	0.647	0.614	0.780	0.656
$\Delta_{0-} \times 10^2$	3.816	3.306	3.079	3.356
$\frac{BR(B \to D\tau\nu)}{BR(B \to De\nu)}$	0.818	0.802	0.843	0.820
R_{l23}	0.345	0.340	0.367	0.347
$BR(D_s \to \tau\nu)$	2.224	2.220	2.238	2.225
$BR(D_s \to \mu\nu)$	3.109	3.106	3.122	3.109
$BR(D \to \mu\nu)$	0.008	0.084	0.008	0.008
$\Omega_\chi h^2$	0.025	0.026	0.056	0.022
m_h	1.022	1.482	1.216	1.297
XENON100	0.042	0.110	0.0	0.165
LHC	0.0	0.0	0.0	0.0
Sparticles	0.0	0.0	0.0	0.0
$BR(\overline{B}_s \to \mu^+\mu^-)$	0.0	0.0	0.0	0.0
Total	15.91	16.62	15.86	16.83
χ^2/dof	1.77	1.85	1.76	1.87

TABLE V: Breakdown of the total χ^2 by observable for the best fit points in our scans, for both cases where the nuisance parameters have been fixed (two left columns) and profiled over (two right columns).
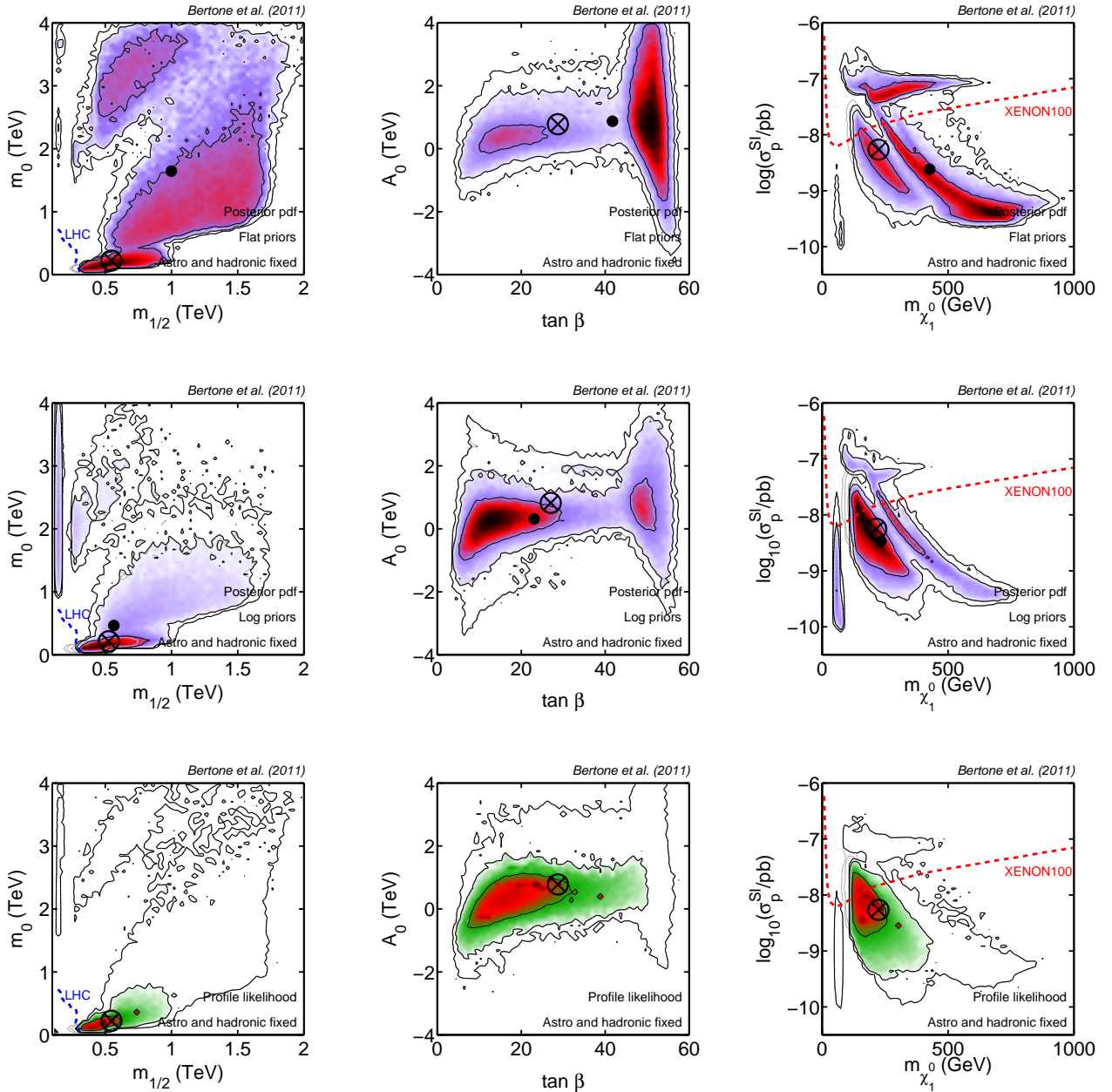
FIG. 1: Black contours: posterior pdf (upper panels, for flat and log priors) and profile likelihood (lower panels) for the cMSSM parameters, including all present-day constraints (WMAP 7-years and LHC first results included), except XENON100. From the inside out, contours enclose 68%, 95% and 99% of marginal posterior probability (top two rows) and the corresponding profiled confidence intervals (bottom panels). The black cross represents the best fit, the black dot the posterior mean (for the pdf plots). Parameters describing astrophysical and hadronic uncertainties have been fixed to their fiducial values. Grey contours (very difficult to see, as they almost overlap with the black contours) represent the constraints obtained without inclusion of LHC data. In the plots on the left, the dashed/blue line represents the current LHC exclusion limit, while in the right-most plots the red/dashed line is the 90% exclusion limit from XENON100, from Ref. [20], rescaled to our fiducial local DM density of $\rho_{\rm loc} = 0.4$ GeV/cm^3.

99% region, whose extent is much larger than would be inferred by assuming an approximately Gaussian distribution from the 68% region. Finally, it is interesting that the extent of the 99% profile likelihood region is actually very similar to the 99% posterior region from the flat

prior scan (compare outer-most contours of the middle and bottom panels of Fig. 1).

We now turn to discuss the best fit points identified in our scans (see Table IV). The contribution of each observable to the best fit χ^2 is shown in Table V, where

the χ^2 is defined as

$$\chi^2 \equiv -2 \sum_i \ln \mathcal{L}_i, \qquad (12)$$

and $\mathcal{L}_i$ is the likelihood for each observable. The likelihood $\mathcal{L}_i$ is normalized in such a way that for Gaussian-distributed data points $\ln \mathcal{L}_i = 0$ when the theoretical value matches the observed mean in Table III. For observables for which only limits exist, the likelihood is normalized so that $\ln \mathcal{L}_i = 0$ asymptotically above/below the stated exclusion limit. The one exception to this is the XENON100 likelihood, which is normalized as explained above, and therefore there is a residual contribution to the χ^2 of ≈ 0.57 units when $s(\boldsymbol{\Theta}) \to 0$ (i.e. for very small interaction cross-sections, $\sigma_{\chi-p}^{\rm SI} \ll 10^{-9}$ pb). In evaluating the number of degrees of freedom (dof), we only count as "active" Gaussian data points (13 in total, from Table III), for 4 cMSSM free parameters (nuisance parameters are not counted as each one of them is independently constrained), thus giving dof = 9. Despite the leakage of probability into the FP discussed above, it is interesting that the best fit points for both the flat and log prior scans are very well compatible, and lie in the bulk region, in contrast to what had been found in Ref. [18, 67], who reported best fits in the FP region based on an older combination of data. Despite this, as discussed above the FP region cannot be excluded at the 99% level either from a Bayesian or a profile likelihood perspective unless one includes in the likelihood direct detection data (see below).

The observables contributing the most to the total χ^2 in Table V, namely the branching ratios of $BR(D_s \to \tau\nu)$ and $BR(D_s \to \mu\nu)$ are sensitive to new physics mainly through the mass of the charged Higgs bosons $H^\pm$ and to some extend to $\tan\beta$ [68], in particular for low $m_{H^\pm}$ and large $\tan\beta$ values. Our best fit points have relatively large $m_{H^\pm}$ and low/intermediate $\tan\beta$, and therefore the theoretical values for those processes are SM-like and have a discrepancy at the $1.5\,\sigma$ level with the experimental values. For the isospin asymmetry Δ_{0-} new physics contributions become important to large $\tan\beta$ and low $m_{1/2}$ [69]. Hence the predictions for our best fit points are again SM-like, showing a discrepancy at the $2\,\sigma$ level with the experimental central values. In constrast, relatively good fits can be found in the bulk region for both the anomalous magnetic moment of the muon and $BR(\bar{B} \to X_s\gamma)$, as can be seen from their relatively low contribution to the total χ^2.

B. Impact of XENON100 for fixed nuisance parameters

We show in Fig. 2 the impact of further adding XENON100 data, and compare the resulting constraints with the case where all constraints are included except XENON100 (gray contours). We keep for the moment all astrophysical and hadronic nuisance parameters fixed to their fiducial values, before moving on to the full analysis. The impact of direct detection data on the posterior pdf with flat priors is fairly dramatic, as can be seen in the three panels of the first row. The most obvious consequence is that the FP becomes strongly disfavoured. In the case of log priors (second row of Fig. 2), the impact of direct detection data is less dramatic on the posterior, but the parameter space shrinks significantly also in this case, a result that clearly demonstrates the potential of direct detection experiments. Overall, we observe that the posterior pdf's for the two choices of priors are now in much better agreement with each other (despite some residual volume effects, which are evident e.g. in the large concentration of probability density for large $\tan\beta$ in the middle panel of the first row), as one would expect when the posterior becomes more and more strongly dominated by the likelihood and the impact of priors is reduced (see Ref. [70] for another example). The profile likelihood 99% region (bottom panels) is also strongly reduced by inclusion of XENON100 data, and it now extends somewhat in-between the 99% posterior region from the flat and the log prior scans.

Regarding prospects for DM direct detection in the cMSSM, by comparing the right-most panels in Fig. 2 we observed that the extension of the favoured region at 99% in the $m_\chi, \sigma_{\chi-p}^{\rm SI}$ plane is now almost independent of the statistical approach and the priors used, a point we will return to in more detail below when we discuss prospects for cMSSM discovery in various observational channels.

C. Influence of hadronic and astrophysical uncertainties.

We present the effect of including hadronic uncertainties in the top panels of Fig. 3. A comparison with the case where the hadronic matrix elements are fixed (grey contours in the figure) shows that although a full analysis leads to slightly more conservative results by increasing slightly the extent of the favoured regions, the simplified analysis with fixed hadronic parameters is accurate enough to draw fairly accurate conclusions on the impact of various searches on the cMSSM parameter space.

Finally, including both sets of nuisance parameters and marginalizing/profiling over them is the most robust way of applying direct detection constraints. This case is presented in the bottom panels of Fig. 3. Again, we observe a slight broadening of the contours for the Bayesian pdf, compared to the case when both sets of nuisance parameters are kept fixed, but the overall impact on the favoured region is quite small. Regarding the profile likelihood depicted in the bottom-right panel of Fig. 3, the profiled contours for the case including nuisance parameters are actually slightly smaller (at 99%) than when the nuisance parameters are held fixed. This is a consequence of the slightly better value for the best fit χ^2 found in our scan including nuisance parameters (cf Table V), compared
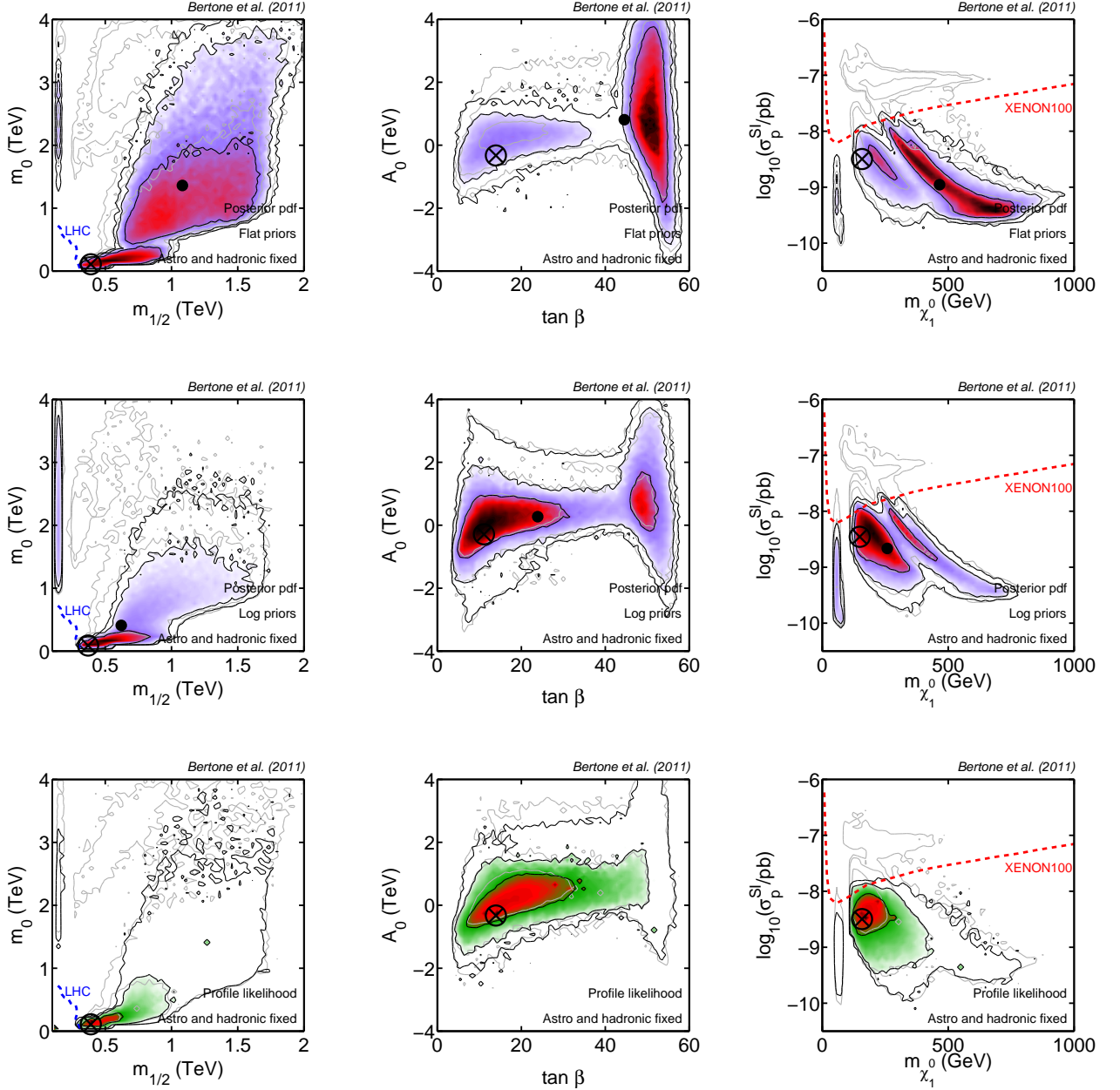
FIG. 2: As in Fig. 1, but now black contours include XENON100 data (for fixed hadronic and astrophysical uncertainties), while the gray empty contours show for comparison the case where no direct detection data are included (from the inside out: 68%, 95% and 99% regions). We observe a strong suppression of the viability of the FP region in the Bayesian posterior (top and middle row), and a better agreement between the posterior distributions and the profile likelihood. Notice that the XENON100 90% limit (red/dashed line) has been included only to guide the eye, as our implementation of the XENON100 data is slightly more conservative than the procedure adopted in Ref. [20].

with the overall best fit when the nuisance parameters are fixed ($\Delta\chi^2 = 0.05$). A detailed analysis reveals that the improvement is largely ascribable to the better $(g-2)_\mu$ value found in the former scan, which is essentially exactly identical to the experimental central value. For the profile likelihood, even a very small improvement in the best fit value has an impact on the contours as far out in the tails as 99%, as those are defined with respect to the

best fit χ^2. However, given the numerical uncertainties associated with any scan, we can safely conclude that this tightening of the contours is a spurious effect and that the extent of the 99% region remains qualitatively the same when including both hadronic and astrophysical nuisance parameters in the scan.
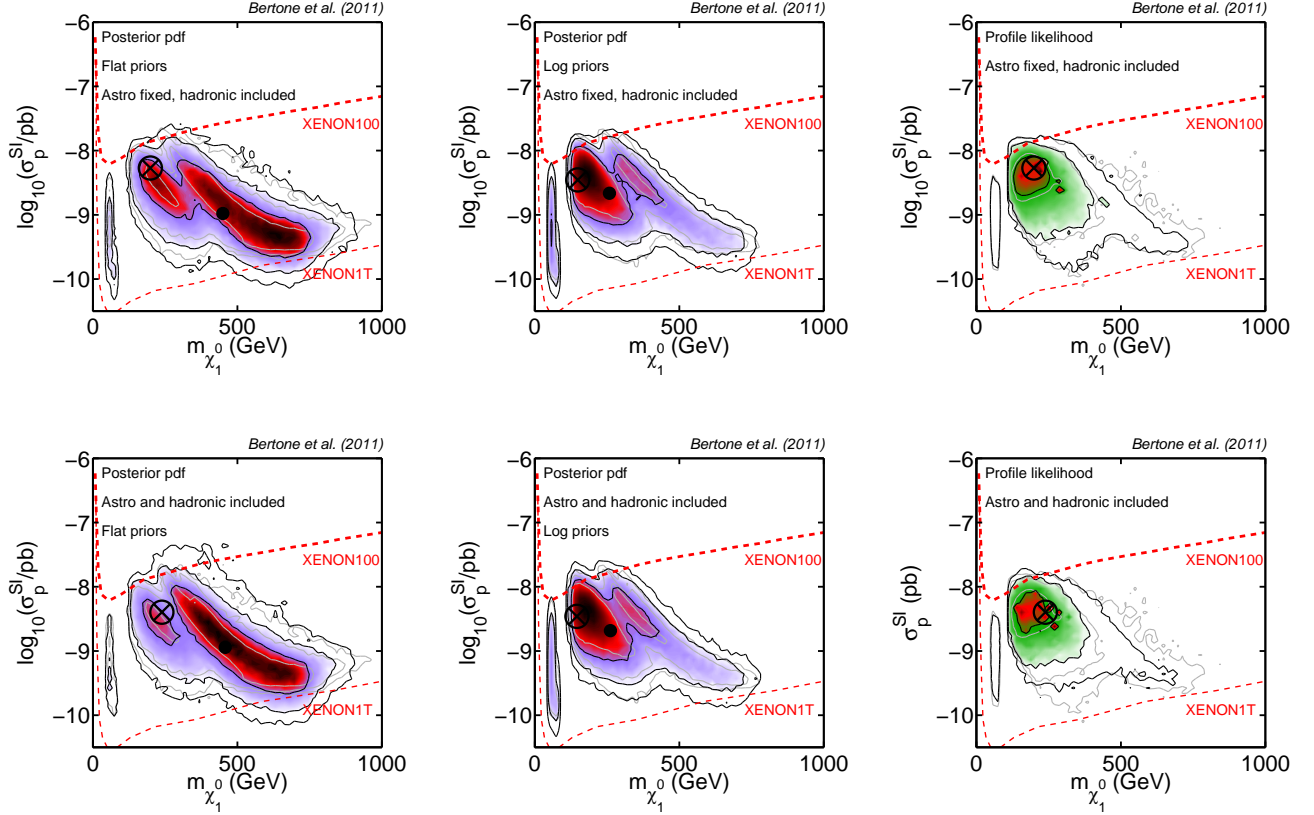
FIG. 3: Top row: Impact of marginalizing (profiling) over hadronic uncertainties as nuisance parameters in the posterior pdf (profile likelihood, right-most panels). Parameters describing astrophysical uncertainties have been fixed to their fiducial values. Bottom row: Impact of further marginalizing/profiling over astrophysical uncertainties. For comparison, the gray contours are the case where both the hadronic and astrophysics nuisance parameters are fixed to their fiducial value. In all panels, all available data have been applied (including LHC and XENON100). The reach of the future ton-scale XENON1T experiment is also indicated (bottom red/dashed line).

V. UPDATED PROSPECTS FOR CMSSM DISCOVERY

We now turn to discuss the implications of our results for detection prospects at the LHC, and via direct and indirect detection channels. Fig. 4 shows 1D posterior distributions and profile likelihoods for the lightest Higgs mass, m_h, the gluino mass $m_{\tilde{g}}$, the neutralino mass $m_{\chi_1^0}$, the spin-independent scattering cross section $\sigma_{\chi-p}^{SI}$ and the spin-dependent scattering cross section of neutralinos off protons $\sigma_{\chi-p}^{SD}$.

We notice that the 1D marginal distributions for the log prior scan (thick solid/red) and the 1D profile likelihood (dashed/black) are very similar, while the 1D distribution from the flat prior scan (thin solid/blue) still shows some residual volume effect. This manifests itself e.g. in the shift of the bulk of the probability density to larger gluino and neutralino masses. However, a robust result of our scans is that the best fit neutralino mass is fairly small (in the range $\sim 150-250$ GeV), the lightest Higgs very light (just above the LEP exclusion limit), and the spin-independent scattering cross section

a mere factor of ~ 2 below current XENON100 limits. This therefore puts our best fit point for the cMSSM easily within reach of the next generation of direct detection experiments. In particular, the upcoming scaled-up version of XENON100, XENON1T, is expected to probe by 2015 practically the entire 99% posterior and profile likelihood shown above, reaching a sensitivity better than $\sigma_{\chi-p}^{SI} = 10^{-10}$ pb in a mass range extending from 20 to 300 GeV (see e.g. the recent assessment of the XENON1T reach in Ref. [71]).

Interestingly, the FP is a region that presents promising prospects for *indirect* DM searches, especially for what concerns the detection of high-energy neutrinos from DM annihilations in the Sun (e.g. Ref. [72, 73]), that should be possible with the IceCube neutrino telescope if the $\sigma_{\chi-p}^{SD}$ is larger than $\approx 3 \times 10^{-5}$ pb (for an observation time of 5 years, and including the densely instrumented region DeepCore at the center of IceCube, see e.g. Ref. [74] for details). The fact that XENON100 rules out the FP branch has therefore a negative impact on the prospects for indirect detection, and further constrains the possibility to probe DM in the cMSSM with
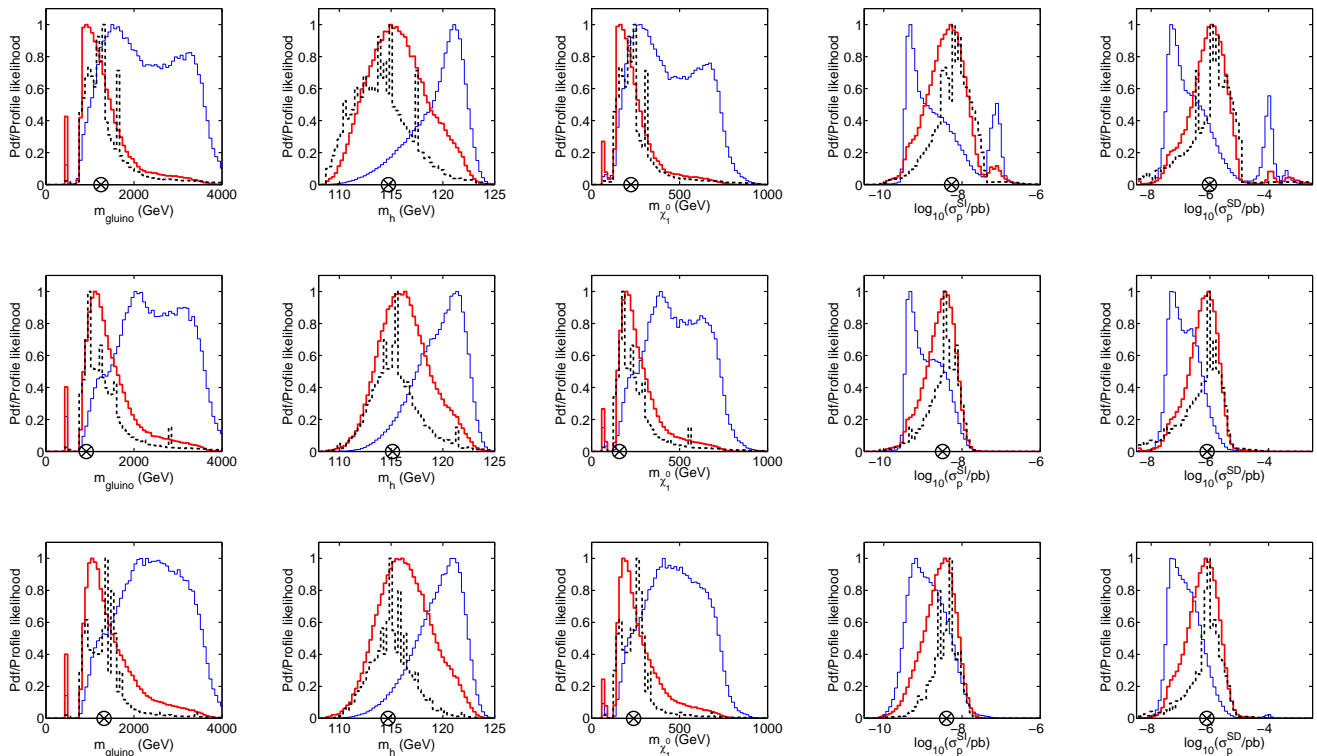
FIG. 4: 1D marginal pdf for flat priors (thin solid/blue), log priors (thick solid/red) and 1D profile likelihood (dashed/black) for the gluino mass, the lightest Higgs mass, the neutralino mass, the SI and the SD scattering cross section (from left to right). Top panels include all data except XENON100, middle panels include XENON100 data and bottom panels further marginalize over hadronic and astrophysical uncertainties. The best fit point is indicated by the encircled black cross.

astrophysical experiments. Upon inspection of the posterior pdf and profile likelihood in the right-most panels of Fig. 4, we see that after inclusion of XENON100 data the region with the highest pdf and profile likelihood values falls below the sensitivity of IceCube, although a detection is still statistically possible in the tails of the distributions but now more unlikely. Finally, comparison of the middle and bottom rows of Fig. 4 shows that inclusion of the astrophysical and hadronic uncertainties does not change the overall conclusions dramatically, with only mild shifts to the resulting inferences resulting from inclusion of the extra nuisance parameters in the scan (bottom row).

VI. CONCLUSION

We have presented in this paper new global fits of the cMSSM, including the most recent constraints from the LHC and the XENON100 experiment. Besides the uncertainties on Standard Model quantities, our analysis takes into account both astrophysical and hadronic uncertainties that enter in the calculation of the rate of WIMP-induced recoils in direct detection experiment. We have shown that the FP branch of the cMSSM is robustly ruled out, even when all uncertainties are taken into account.

Although our results are specific to the cMSSM, we note that the conditions for the occurrence of the FP can actually be extended to a general class of unconstrained Supersymmetric scenarios. In models where no universality assumptions on the soft mass parameters are made, the FP region can be shifted to either larger or lower scalar mass parameters, but the general feature of the smallness of the μ parameter is preserved, as are its implications for dark matter. In Ref. [72], for example, a low-energy parametrization of the FP was studied that could be used to describe this region irrespectively of the high-energy assumptions. Although the analysis of these general constructions is beyond the scope of the present work, it seems reasonable to extend our conclusions to the general case, given the similarity of the predicted direct detection rates.

While this work was under completion, Refs. [62, 75] performed a similar analysis of the impact of LHC and XENON100 data on the parameter space of several theoretical models, including the cMSSM. While our results about the viability of the FP regions are qualitatively similar, our analysis differs from that in the above references in that we studied the impact of both hadronic and astrophysical uncertainties (both neglected in Ref. [75], while Ref. [62] includes only hadronic uncertainties). Furthermore, we adopt a more sophisticated

statistical framework than Ref. [75] (which only excluded points in parameter space with hard cuts, rather than proper likelihood functions, and which did not perform a statistical scan of the parameter space) and perform a detaild, quantitative comparison between the Bayesian and profile likelihood results (absent in Ref. [62]).

[1] A. H. Chamseddine, R. L. Arnowitt and P. Nath, Phys. Rev. Lett. **49** (1982) 970.

[2] G. L. Kane, C. F. Kolda, L. Roszkowski and J. D. Wells, Phys. Rev. D **49** (1994) 6173

[3] *Particle Dark Matter: Observations, Models and Searches*, ed. G. Bertone, Cambridge University Press (2010)

[4] L. Bergstrom, Rept. Prog. Phys. **63**, 793 (2000)

[5] C. Munoz, Int. J. Mod. Phys. A **19**, 3093 (2004)

[6] G. Bertone, D. Hooper and J. Silk, Phys. Rept. **405**, 279 (2005)

[7] S. Chatrchyan *et al.* [CMS Collaboration], [arXiv:1103.0953 [hep-ex]].

[8] V. Khachatryan *et al.* [CMS Collaboration], Phys. Lett. **B698** (2011) 196-218.

[9] G. Aad *et al.* [Atlas Collaboration], [arXiv:1102.5290 [hep-ex]].

[10] G. Aad *et al.* [ATLAS Collaboration], arXiv:1103.4344 [hep-ex].

[11] G. Aad *et al.* [ATLAS Collaboration], arXiv:1103.6214 [hep-ex].

[12] O. Buchmueller, R. Cavanaugh, D. Colling, A. De Roeck, M. J. Dolan, J. R. Ellis, H. Flacher, S. Heinemeyer *et al.*, [arXiv:1102.4585 [hep-ph]].

[13] B. C. Allanach, [arXiv:1102.3149 [hep-ph]].

[14] S. Akula, D. Feldman, Z. Liu, P. Nath, G. Peim, [arXiv:1103.5061 [hep-ph]].

[15] A. Strumia, [arXiv:1101.2195 [hep-ph]].

[16] R. Ruiz de Austri, R. Trotta and L. Roszkowski, JHEP **0605**, 002 (2006)

[17] R. Trotta, F. Feroz, M. P. Hobson, L. Roszkowski and R. Ruiz de Austri, JHEP **0812** (2008) 024

[18] F. Feroz, K. Cranmer, M. Hobson, R. Ruiz de Austri and R. Trotta, JHEP in print, arXiv:1101.3296 [hep-ph].

[19] D. G. Cerdeño and A. M. Green, arXiv:1002.1912 [astro-ph.CO].

[20] E. Aprile *et al.* [XENON100 Collaboration], arXiv:1104.2549 [astro-ph.CO].

[21] L. Roszkowski, R. Ruiz de Austri and R. Trotta, JHEP **0707**, 075 (2007)

[22] The CDF Collaboration and D0 Collaboration, *A Combination of CDF and D0 Results on the Mass of the Top Quark* arXiv:0903.2503 [hep-ex].

[23] W.-M. Yao *et al.*, J. Phys. **G33** (2006).

[24] K. Hagiwara, A. D. Martin, D. Nomura and T. Teubner, Phys. Lett. B **649**, 173 (2007).

[25] M. Pato, L. Baudis, G. Bertone, R. Ruiz de Austri, L. E. Strigari, R. Trotta (2011), Phys. Rev. D in print, [arXiv:1012.3458 [astro-ph.CO]].

[26] J. R. Ellis, K. A. Olive and C. Savage, Phys. Rev. D **77**, 065026 (2008)

[27] R. Trotta, Contemp. Phys. **49**, 71 (2008)

[28] P. Scott, J. Conrad, J. Edsjo, L. Bergstrom, C. Farnier and Y. Akrami, JCAP **1001** (2010) 031

[29] Avaiable from: `http://superbayes.org/`

[30] F. Feroz and M. P. Hobson, Mon. Not. Roy. Astron. Soc. **384** (2008) 449–463.

[31] F. Feroz, M. P. Hobson, and M. Bridges, Mon. Not. Roy. Astron. Soc. **398** (2009) 1601–1614.

[32] P. Gondolo, J. Edsjö, P. Ullio, L. Bergstrm̈, M. Schelke, E.A. Baltz, T. Bringmann and G. Duda, `http://www.darksusy.org/`

[33] P. Gondolo, J. Edsjo, P. Ullio, L. Bergstrom, M. Schelke and E. A. Baltz, JCAP **0407** (2004) 008

[34] `http://projects.hepforge.org/softsusy/`

[35] B. C. Allanach, Comput. Phys. Commun. **143** (2002) 305

[36] `http://lapth.in2p3.fr/micromegas/`

[37] G. Belanger, F. Boudjema, A. Pukhov and A. Semenov, Comput. Phys. Commun. **176** (2007) 367

[38] `http://superiso.in2p3.fr/`

[39] F. Mahmoudi, Comput. Phys. Commun. **180**, 1579 (2009)

[40] G. Degrassi, P. Gambino and P. Slavich, Comput. Phys. Commun. **179** (2008) 759

[41] `http://slavich.web.cern.ch/slavich/susybsg/`

[42] G. Degrassi, P. Gambino and P. Slavich, Phys. Lett. B **635** (2006) 335

[43] G. D'Ambrosio, G. F. Giudice, G. Isidori and A. Strumia, Nucl. Phys. B **645**, 155 (2002)

[44] G. Aad *et al.* [Atlas Collaboration], arXiv:1102.2357 [hep-ex].

[45] `http://lepewwg.web.cern.ch/LEPEWWG`.

[46] M. Davier *et al.*, In Proceedings of "TAU 2010 - The 11th International Workshop on Tau Lepton Physics", Manchester, UK, 13 - 17 September 2010, arXiv:0906.5443 [hep-ph].

[47] Heavy Flavor Averaging D. Asner *et al.*, arXiv:1010.1589

[48] The CDF Collaboration, Phys. Rev. Lett., 97, (2006), 062003.and Phys. Rev. Lett., 97, (2006), 242003.

[49] B. Aubert *et al.* [BABAR Collaboration], arXiv:0808.1915 [hep-ex].

[50] B. Aubert *et al.* [BABAR Collaboration], Phys. Rev.

Lett. **100** (2008) 021801

[51] M. Antonelli *et al.* [FlaviaNet Working Group on Kaon Decays], arXiv:0801.1817 [hep-ph].

[52] N. Jarosik *et al.*, Astrophys. J. Suppl. **192** (2011) 14

[53] The CDF Collaboration, Phys. Rev. Lett. 972006242003.

[54] G. Abbiendi *et al.* [the ALEPH Collaboration, the DELPHI Collaboration, the L3 Collaboration and the OPAL Collaboration, The LEP Working Group for Higgs Boson Searches], Phys. Lett. B **565**, 61 (2003)

[55] G. Bertone, D. G. Cerdeño, M. Fornasa, R. Ruiz de Austri and R. Trotta, Phys. Rev. D **82** (2010) 055008

[56] L. E. Strigari and R. Trotta, JCAP **0911**, 019 (2009)

[57] G. Duda, A. Kemper and P. Gondolo, JCAP **0704** (2007) 012

[58] M. Lisanti, L. E. Strigari, J. G. Wacker *et al.*, [arXiv:1010.4300 [astro-ph.CO]].

[59] C. Arina, J. Hamann, Y. Y. Y. Wong, [arXiv:1105.5121 [hep-ph]].

[60] E. Aprile *et al.* [XENON100 Collaboration], [arXiv:1103.0303 [hep-ex]].

[61] B. C. Allanach, T. J. Khoo, C. G. Lester, S. L. Williams, [arXiv:1103.0969 [hep-ph]].

[62] O. Buchmueller *et al.*, arXiv:1106.2529 [hep-ph].

[63] J. L. Feng, K. T. Matchev and T. Moroi, Phys. Rev. D **61**, 075005 (2000)

[64] J. L. Feng, K. T. Matchev and F. Wilczek, Phys. Lett. B **482**, 388 (2000)

[65] K. L. Chan, U. Chattopadhyay and P. Nath, Phys. Rev. D **58**, 096004 (1998)

[66] H. Baer and M. Brhlik, Phys. Rev. D **57**, 567 (1998)

[67] Y. Akrami, P. Scott, J. Edsjo, J. Conrad, L. Bergstrom, JHEP **1004**, 057 (2010).

[68] A. G. Akeroyd and F. Mahmoudi, JHEP **0904** (2009) 121

[69] M. R. Ahmady and F. Mahmoudi, Phys. Rev. D **75** (2007) 015007

[70] L. Roszkowski, R. Ruiz de Austri and R. Trotta, Phys. Rev. D **82** (2010) 055003

[71] E. Aprile et al. (XENON1T Collaboration), XENON1T at LNGS, Proposal, April (2010) and Technical Design Report, October (2010).

[72] H. Baer, T. Krupovnickas, S. Profumo and P. Ullio, JHEP **0510**, 020 (2005)

[73] R. Trotta, R. Ruiz de Austri, C. P. d. l. Heros, JCAP **0908** (2009) 034.

[74] F. Halzen and D. Hooper, New J. Phys. **11** (2009) 105019

[75] M. Farina, M. Kadastik, D. Pappadopulo, J. Pata, M. Raidal, A. Strumia, [arXiv:1104.3572 [hep-ph]].